ADVANCED FUNCTIONAL MATERIALS
www.afm-journal.de

Oxygen Reduction Reaction Performance of [MTBD][beti]-Encapsulated Nanoporous NiPt Alloy Nanoparticles

*Joshua Snyder, Kenneth Livi, and Jonah Erlebacher**

Recent advances in oxygen reduction reaction catalysis for proton exchange membrane fuel cells (PEMFCs) include i) the use of electrochemical dealloying to produce high surface area and sometimes nanoporous catalysts with a Pt-enriched outer surface, and ii) the observation that oxygen reduction in nanoporous materials can be potentially enhanced by confinement effects, particularly if the chemical environment within the pores can bias the reaction toward completion. Here, these advances are combined by incorporating a hydrophobic, protic ionic liquid, [MTBD][beti], into the pores of high surface-area NiPt alloy nanoporous nanoparticles (np-NiPt/C + [MTBD][beti]). The high O_2 solubility of the [MTBD][beti], in conjunction with the confined environment within the pores, biases reactant O_2 toward the catalytic surface, consistent with an increased residence time and enhanced attempt frequencies, resulting in improved reaction kinetics. Half-cell measurements show the np-NiPt/C+[MTBD][beti] encapsulated catalyst to be nearly an order of magnitude more active than commercial Pt/C, a result that is directly translated into operational PEMFCs.

1. Introduction

Recent developments in fuel cell catalyst and catalyst layer technology have focused on changes in electrocatalyst composition, nanostructure and support composition and morphology. For instance, alloying of Pt with transition metals[1–10] or forming Pt-skinned or core-shell nanostructures[11–18] further improve catalyst activity by adjusting the oxygen reduction reaction (ORR) kinetics through optimized interaction between the catalyst and reactant O_2. One common approach to the synthesis of such materials involves electrochemical dealloying in which the less-noble component of an alloy nanoparticle (e.g., Cu, Ni, Co) is dissolved away under conditions where the remaining component (e.g., Pt) is mobile via surface diffusion, and re-organizes to form a passivating and catalytically active layer over a bulk composition containing a significant residual fraction of the transition metal alloying component.[15–17,19,20] Underlying transition metals create a shift in the electronic (d-band center) and the geometric structure of Pt surface atoms, limiting the surface coverage of ORR intermediate species and increasing the number of available active sites.[2,21] When applied to sub ≈10 nm nanoparticles, dealloying generally leads to compact particles with a core-shell structure.[15,22,23] When applied to larger particles, dealloying can lead to the formation of "nanoporous nanoparticles", in which porosity at the 3-4 nm scale is entrained within particles of ≈15 nm diameters; see for instance our detailed study of the ORR activity of nanoporous Ni/Pt nanoparticles.[22] These particles have surface area to volume ratios comparable to small nanoparticles and the high mass activities of Pt-shell, Pt/transition metal alloy-core nanoparticles.

Porosity adds a design feature missing in smaller compact nanoparticles; namely, the pores can be filled with secondary materials that can bias the oxygen reduction reaction toward completion. In previous work,[20] we showed in half-cell electrochemical measurements that bulk samples of dealloyed, nanoporous Ni/Pt filled with a hydrophobic, protic ionic liquid (IL, an ionic salt that is liquid at room temperature, formed by neutralization of a Brønsted acid with a Brønsted base) had significantly higher mass and specific activity than the dealloyed, nanoporous material alone. Our working model for the increase in activity is essentially a confinement effect: if a porous Pt catalyst operating in an aqueous environment is encapsulated in a second phase material whose role is to maintain a higher O_2 concentration at the catalyst surface (equivalently, O_2 residence time), then one can expect that at low overpotential, that is, relatively high voltages where the ORR is not mass transported-limited by O_2, the activity will be multiplied by a factor equal to the ratio of solubilities between the IL and the exterior water phase. Thermodynamically, the encapsulation medium changes the chemical potential gradient for oxygen diffusion toward the catalyst surface (not the total driving force for the overall reaction, which is determined by the electrochemical potential), biasing O_2 to remain near the catalyst surface, increasing residence time and attempt frequency for the reduction reaction. This picture was consistent with the experimental observations. Bulk materials, however, are subject to mass transport limitations, especially at high overpotential. In a previous study,[20] we found that the mass activity of the IL-filled catalyst decreased

Dr. J. Snyder, Dr. J. Erlebacher
Department of Materials Science and Engineering &
Department of Chemical and Biomolecular Engineering
Johns Hopkins University
Baltimore, MD 21218, USA
E-mail: jonah.erlebacher@jhu.edu
Dr. K. Livi
Department of Earth and Planetary Sciences
Johns Hopkins University
Baltimore, MD 21218, USA

DOI: 10.1002/adfm.201301144

with increasing depth of porosity due to a transport resistance of reactant O_2 and, beyond a few tens of nanometers depth, the catalytic surface was functionally inactive. Here, we show that the concept of impregnating a nanoporous catalyst with a suitable IL can be combined with the synthesis of nanoporous nanoparticles to create an IL-encapsulated Ni/Pt nanoporous nanoparticle catalyst supported on carbon (np-NiPt/C+IL). The half-cell specific activity of this catalyst architecture was found to be an order of magnitude higher than that of commercial Pt/C. As hypothesized, np-NiPt/C+IL catalysts did not seem to suffer from the mass transport limitations of the bulk material because the depth of porosity was sufficiently small. We present preliminary fuel cell measurements that suggest the half-cell improvements using this composite catalyst are directly translated into working proton exchange membrane fuel cells (PEMFCs), opening up a significant new direction for oxygen reduction catalyst design.

2. Results and Discussion

Figure 1A contains a representative schematic illustrating the key components of our encapsulated catalyst and Figure 1B is a transmission electron microscopy (TEM) image of encapsulated nanoporous catalyst particles. The nucleus of the catalyst is a high surface area Ni/Pt nanoporous nanoparticle (np-NiPt) made by synthesizing ≈15 nm diameter $Ni_{75}Pt_{25}$ nanoparticles via a solvothermal method,[22] supporting them on carbon, thermally homogenizing the alloy nanoparticles, and subsequently dealloying them via potential cycling in 0.1 M $HClO_4$. This process led to porous particles, with pore and ligament sizes of ≈3–4 nm, a surface passivated with Pt, and a residual average composition of ≈Pt_3Ni. These particles were encapsulated by drying a dispersion of the IL [7-methyl-1,5,7-triazabicyclo[4.4.0]dec-5-ene, MTBD][bis(perfluoroethylsulfonyl)imide, beti] in ethanol over the catalyst. The wetting characteristics of the np-NiPt nanoparticles and carbon support were such that the IL preferentially encapsulated the metal nanoparticles. In fact, the IL is clearly shown as an amorphous halo surrounding the nanoporous nanoparticles in Figure 1B, a feature not seen in the TEM of bare nanoparticles, see Figure S1 in Supporting Information. (Note an advantageous quality of ILs is their nearly nonexistent vapor pressure, meaning the IL will not evaporate during fuel cell operation at elevated temperature and also that the IL can be imaged under vacuum in electron microscopy.) The protic [MTBD][beti] IL has an oxygen solubility ≈2.4 times that of a dilute acidic solution,[20] an adequate electrochemical potential stability window encompassing both anodic (H_2) and cathodic (O_2) potentials relevant to PEMFC operation and is highly hydrophobic and thermally stable beyond 150 °C.[24]

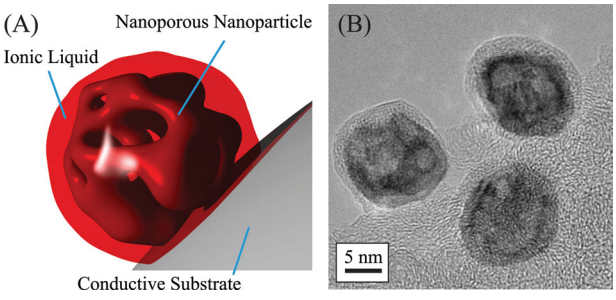

Figure 1. Schematic and implementation of encapulsated nanoporous nanoparticle catalysts for high-performance PEMFC oxygen reduction. A) Cartoon illustrating the key components: the nucleus of the catalyst is a high surface area nanoporous nanoparticle, which allows the particle to be encapsulated by an IL. The composite catalyst is attached to a conductive substrate to aid integration into a PEMFC cathode catalyst layer. B) High resolution transmission electron microscope image (HRTEM) of nanoporous nickel-platinum (np-NiPt) nanoparticles encapsulated with [MTBD][beti] IL, supported on carbon. This protic, hydrophobic IL increases the residence time of oxygen near the catalyst surface, improving activity.

Figure 2A contains the representative cyclic voltammograms (CV) for commercial 20 wt% Pt/C, np-NiPt/C and np-NiPt/C+[MTBD][beti]. We see a clear positive shift in the initiation potential of Pt-oxide formation for np-NiPt/C catalysts with the degree of Pt oxidation lowest for the np-NiPt/C+[MTBD][beti] encapsulated catalyst, which is a consequence of the nonaqueous environment provided by the IL. Suppression of Pt oxide formation improves ORR activity by decreasing active site blocking by OH_{ad} species. It is important to note that the CV for np-NiPt/C+[MTBD][beti] shows no extra Faradaic processes other than those that typically occur on Pt and Pt alloys, hydrogen underpotential deposition (H_{UPD}) and Pt oxidation, indicating that there is likely no adsorption, reversible or irreversible, of ions from the IL onto the Pt surface. This is in contrast to imidazolium-based ILs, where free imidazole has been known to irreversibly adsorb onto Pt surfaces.[25,26] The nearly identical H_{UPD} region is further evidence that there is little to no site blocking. In this way, the IL is acting simply as a non-interacting electrolyte. The presence of fully formed H_{UPD} peaks and the failure to completely suppress Pt oxidation are an indication of a significant presence of water in the IL. This is not unexpected as the encapsulated catalyst is in direct contact/equilibrium with the acid electrolyte and water equilibrated protic ILs, even hydrophobic protic ILs, are known to contain water concentrations as high as 1 M.[27] CVs in [MTBD][beti] immediately upon immersion in acid, prior to reaching an equilibrium with the aqueous electrolyte (Figure S2, Supporting Information) show significantly suppressed H_{UPD} and Pt oxidation currents due to the low water content of the IL; protons in this case are supplied exclusively by protonated amine sites present near the surface, and the lower currents are an indication of the low protonic concentration. Protic ILs have been used as non-humidified electrolytes for fuel cells, where protons created by oxidation of hydrogen at the anode are shuttled by a Grotthuss mechanism to the cathode at sufficient rates for the ORR. Unfortunately, the proton conductivity was still much lower than that in hydrated Nafion and the overpotential for ORR on Pt in the dry protic ILs was found to be higher than that in acid electrolytes.[25,28,29] Experimental/computational[27,30,31] studies of IL/water mixtures have shown a biphasic, interconnected nanostructure beginning to appear at moderate concentrations of water, 0.3 mole fraction, and a fully connected, percolating network of water at higher concentrations, >0.7 mole fraction, similar to that found in hydrated Nafion.[32,33] Water is likely to be found in the first solvation shell of both the cation and anion, especially the anion, reducing caging effects and viscosity of the IL resulting in improved ionic conductivity and higher rates of

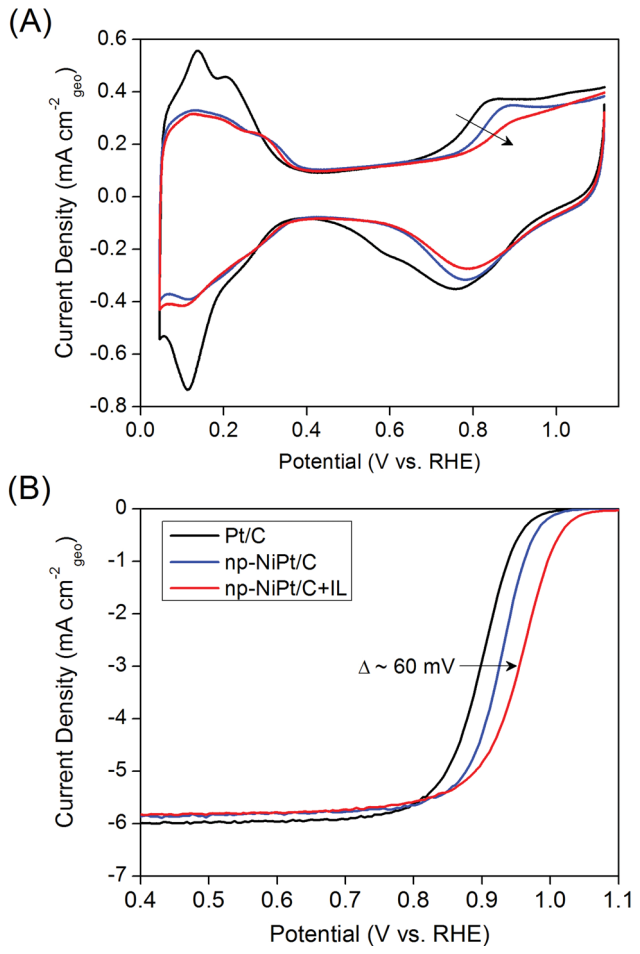

Figure 2. Half-cell electrochemistry of encapsulated nanoporous nanoparticle catalysts. A) Cyclic voltammograms (CVs) of 20 wt% Pt/C (black line), np-NiPt/C (blue line), and np-NiPt/C+[MTBD][beti] (red line), recorded in deaerated 0.1 M $HClO_4$ at room temperature with a sweep rate of 50 mV s^{-1}. B) Oxygen reduction reaction (ORR) curves for 20 wt% Pt/C (black line), np-NiPt/C (blue line), and np-NiPt/C+[MTBD][beti] (red line), recorded in O_2 saturated 0.1 M $HClO_4$ at 60 °C, with a sweep rate of 20 mV s^{-1} and a rotation rate of 1600 rpm. Loading on the glassy carbon disk in all cases was 12 μg_{Pt} cm^{-2}. Potentials were corrected for iR drop (25 Ω) within the electrolyte. Currents are reported as current density per geometric area of disk. In (A), the arrow indicates a significant increase in the onset potential for platinum oxidation due to both the Pt-skeleton alloy structure of the catalyst and encapsulation with the IL. This decrease in OH_{ad} surface coverage is reflected, in conjunction with the higher O_2 concentration in the IL phase, in a ≈60 mV reduction in the overpotential for oxygen reduction (i.e., from the standard reaction potential of 1.2 V), as shown in (B) where the half-wave has shifted to 0.96 V vs. RHE.

O_2 diffusion.[31,34,35] The presence of water in the acid equilibrated [MTBD][beti] IL aids protonic transport, with hydronium ions diffusing through water channels, vehicular diffusion, in the IL in addition to proton hopping/exchange, Grotthuss diffusion, between hydronium and water molecules and along the amine sites of the [MTBD], similar to the mechanism of protonic transport in hydrated Nafion;[36,37] however the amount of water uptake is considerably lower in the IL than in hydrated Nafion.[32,38] In this way, the protic nature of the IL facilitates protonic transport, especially at rates required for the ORR, by allowing a certain concentration of water within the IL rather than relying solely on proton hopping along the protic sites of the IL. This has a direct consequence on the mechanism of the ORR within the encapsulated catalysts.

Figure 2B contains the ORR polarization curves in O_2 saturated 0.1 M $HClO_4$ at 60 °C for commercial 20 wt% Pt/C, np-NiPt/C, and npNiPt/C+[MTBD][beti]. The np-NiPt/C catalyst is considerably more active for the ORR than commercial catalyst as evidenced by the significant reduction in overpotential. The Pt surface area and mass normalized activities for the catalysts at 25 °C and 60 °C are summarized in **Table 1**; all activity numbers are an average of at least three independently synthesized samples. At 0.95 V versus the reversible hydrogen electrode (RHE), our np-NiPt/C catalysts are more than six times as active as Pt/C, where our iR-corrected values for 20 wt% Pt/C are in agreement with other data reported in the literature.[39–42] However, this factor of activity increase is common for NiPt alloys[3–5,8–10,16,17] as well as other nanoporous/dealloyed catalysts[43–47] and is a result of the lower degree of surface passivation by OH_{ad} species due to a shift in the electronic and geometric structure of the active, surface Pt atoms induced by the underlying transition metal alloying component. Integration of the [MTBD][beti] into the np-NiPt nanoparticles resulted in a further increase in activity, where, in agreement with previous results for planar, porous electrodes,[20] the ratio of specific activity for the bare np-NiPt/C and encapsulated catalyst at 0.95 V versus RHE is within error of the ratio of reactant O_2 solubilities in [MTBD][beti] and a 0.1 M acid electrolyte, a factor of ≈2.4. Together, the encapsulated catalysts have an activity near an order of magnitude larger than that for commercial Pt/C catalysts. Our results are consistent with our working model for the IL-impregnated catalysts, namely that the enhanced kinetics are due to an adjustment of the attempt frequency, not a change in an activation barrier for the reaction. By entrapping the reactant near the catalytic surface and increasing its concentration relative to that in the bulk solution, the IL acts to increase the reactant residence time in close proximity to the catalytic surface, increasing both attempt frequency and probability of reaction. Suppression of Pt oxidation at low overpotentials likely also contributes to the improved activity in the composite catalyst.

The ORR in dry aprotic ILs is a 1 e^- process yielding a stable superoxide species, O_2^-, and that in water equilibrated aprotic ILs can yield H_2O_2 as the product through a 2 e^- reduction.[27,48] In contrast, ORR in protic ILs, especially protic ILs in the presence of a moderate concentration of water, with a continuous supply of protons, in the half-cell from the acid electrolyte and in the fuel cell from the anodic oxidation of H_2, can proceed through the optimal 4 e^- pathway that is typical for Pt surfaces[27] as we have shown previously for our nanoporous metal/IL composite catalysts.[20] The seemingly contradictory behavior of the IL as being hydrophobic but having the capability to retain a significant concentration of water should facilitate expulsion of most of the product water, preventing the buildup of that water which may push the hydrophobic IL out of the pores. The advantage of the nanoporous structure for these encapsulated catalysts is two-fold: i) the pores aid in the retention of the IL and facilitate a more favorable interaction between the IL and the surface of the catalyst, preventing it from being completely

Table 1. Specific and mass activity numbers for 20 wt% Pt/C, np-NiPt/C, and np-NiPt/C+[MTBD][beti] IL measured in the half cell at 60 °C (top row in each cell) and 25 °C (bottom row in each cell), in O_2 saturated 0.1 M $HClO_4$ with a sweep rate of 20 mV s^{-1} and a rotation rate of 1600 rpm; catalyst loading on glassy carbon disk was 12 μg_{Pt} cm^{-2}. Potentials were corrected for iR drop (25 Ω) within the electrolyte. Each data point is an average of at least three independent experiments. Note the nearly order-of-magnitude increase in both specific and mass activity from Pt/C to the encapsulated nanoporous nanoparticle catalyst.

		0.9 V vs. RHE		0.95 V vs. RHE	
	ECSA [m^2 g_{Pt}^{-1}]	Specific Activity [mA cm_{Pt}^{-2}]	Mass Activity [mA μg_{Pt}^{-1}]	Specific Activity [mA cm_{Pt}^{-2}]	Mass Activity [mA μg_{Pt}^{-1}]
Pt/C	63 ± 1.8	0.65 ± 0.07 (60 °C)	0.41 ± 0.06	0.080 ± 0.006	0.050 ± 0.006
		0.51 ± 0.01 (25 °C)	0.32 ± 0.01	0.072 ± 0.001	0.044 ± 0.001
np-NiPt/C	41 ± 1.5	3.34 ± 0.39	1.32 ± 0.22	0.49 ± 0.02	0.197 ± 0.004
		2.66 ± 0.07	1.09 ± 0.03	0.35 ± 0.01	0.145 ± 0.005
np-NiPt/C+IL	41 ± 1.5	5.74 ± 0.19	2.19 ± 0.07	1.41 ± 0.05	0.54 ± 0.02
		4.08 ± 0.30	1.68 ± 0.12	0.91 ± 0.03	0.37 ± 0.01

washed away during rotation in the half-cell and under flowing, humidified gas in a PEMFC catalyst layer. The positive shift in half-wave potential when IL is incorporated into np-NiPt/C, ≈30–40 mV, is larger than that seen for Pt/C with IL, ≈10–15 mV, see Figure S3, Supporting Information. This suggests that the porosity yields a more favorable interaction with the IL. ii) The pores may also produce a nanoconfinement effect,[22,49,50] where simply the structure can lead to entrapment of reactant species and higher attempt frequencies, compounding with the effect of the high O_2 concentration in the IL. We have seen this effect when comparing np-NiPt/C catalysts with solid NiPt/C catalysts having identical compositions and electrochemically active surface areas (ECSA); the porous catalyst was found to have a significantly higher activity.[22] Our approach to catalyst design is in contrast to most others where catalyst architecture is tuned to optimize the activation barrier for the reaction or adjust the surface coverage of an undesirable species. By targeting the attempt frequency of the reaction, activity of the composite catalyst is now tied to the IL phase, where improvements are proportional to the O_2 solubility of the IL.

If the ORR enhancement in the composite electrocatalyst is a consequence of the higher O_2 solubility/concentration in the IL phase, then it may be argued that the same enhancement should be seen with a Nafion film on Pt and Pt alloy electrodes, both planar and nanoparticulate; after all, investigations of O_2 transport through Nafion membranes have reported O_2 solubilities as high as 20 times that of water.[51] However, the structure of an extruded Nafion membrane can be significantly different from recast Nafion found in PEMFC catalyst layers, and there are many critical steric and chemical differences between Nafion and the IL used here. In the case of recast Nafion, O_2 solubilities are only 2 to 4 times that in water, where O_2 tends to associate with the fluorines on the polytetrafluoroethylene backbone of Nafion.[52–55] In fact, previous half-cell studies of ORR on Pt electrodes coated with thin Nafion films found a slight improvement in activity at low overpotentials, attributed to the higher O_2 solubility.[52,53] However, at high overpotentials the diffusion limited current was severely decreased due to an O_2 transport resistance through the film. These authors used sulfuric and phosphoric acid electrolytes whose anions are known to strongly adsorb onto the surface of Pt, blocking active sites. More recent investigations of thin Nafion films on Pt single crystal electrodes in a non-adsorbing electrolyte, $HClO_4$, reported a decrease in activity at all potentials for electrodes coated with a Nafion film. This decrease in activity was shown to be a consequence of irreversible adsorption of sulfonate anions from the Nafion polymer matrix along with physical site blocking by the polytetrafluoroethylene backbone; 15 to 20% of active surface sites were rendered inactive.[52,56–58] In the previous studies, the adsorption of bisulfate and phosphate anions at the Nafion/Pt interface likely masked any effect of sulfonate adsorption and therefore the Nafion film appeared to either not inhibit or even slightly improve the ORR. Electrochemistry at the Nafion/metal interface is strongly dependent on the structure of Nafion and how it interacts with the electrolyte. Hydrated Nafion is known to have a micellar structure where the hydrophobic fluorinated polymer chains aggregate and the charged sulfonate groups associate with the water phase.[32,33] O_2 resides with the fluorine of the polymer backbone which is separated from the water phase; therefore, it is likely that the O_2 concentration in the water phase is not much higher than that in the bulk electrolyte. In a protic IL/water mixture, water molecules are intimately associated with the fluorinated anion due to its acidic site and so, in this case, the water should reflect the higher O_2 concentration present in the IL. Nafion integration into the porous catalyst is also limited; whereas with the nanoporous nanoparticles capillary forces easily pull the IL into the pores, full integration of Nafion into the depths of a nanoporous nanoparticle is not possible as the hydrodynamic radius of Nafion is too large, on the order of 10^3 nm.[59]

Unlike rotating disk electrode experiments, functional PEMFC catalyst layers must be designed to address issues related to mass transport of reactant gas, conduction of electrons and proton transport to the catalyst surface, as well as management of product water. With the goal of optimizing the interface of these processes, the advantages of our encapsulated catalyst architecture are clear: i) the hydrophobic nature of the IL should prevent buildup of copious amounts of water on the surface of the catalyst; ii) the protic nature and nominal water content of the IL will aid proton conductivity to catalytic surface sites, especially within the interior of the porous particles; iii) compared to traditional carbon supported nanoparticles, the nanoporous nanoparticles used here are an order of magnitude larger, even though their porosity allows them to have Pt ECSAs nearly as high as commercial catalyst. This geometric feature should limit diffusion and sintering of catalyst nanoparticles on the surface of the carbon supports, which is one of the main degradation and ECSA loss mechanisms for Pt/C;[60–62] iv) as determined in the half-cell, the mass and specific activity are significantly improved through IL encapsulation of the nanoporous nanoparticles. We now discuss results of the IL-encapsulated nanoporous nanoparticle catalyst incorporated into PEMFCs. A caveat: the membrane electrode assemblies

(MEAs) made here are not industrial-class. Catalyst layers were hand-painted, and relatively thick Nafion membranes were used to limit crossover and ease fabrication. However, MEAs using all three catalysts examined, Pt/C, np-NiPt/C, and np-NiPt/C+[MTBD][beti] were made in exactly the same way, with exactly the same catalyst loading (0.2 mg_{Pt} cm^{-2}) at the cathode. One can thus be reasonably confident that the significant improvement we see using our new catalysts can be expected to translate into industrial-class MEAs made using more advanced methods.

PEMFC polarization curves for commercial Pt/C, np-NiPt/C, and np-NiPt/C+[MTBD][beti] are shown in **Figure 3**. Polarization curves were only recorded after 3000 potential hold steps, which while not representative of a true stability analysis, the performance after this initial break-in period indicated that the IL was neither washed away from the catalyst nor were the ionic species electrochemically reduced. Compared to commercial Pt/C, np-NiPt/C demonstrated a considerable increase in current density at all potentials within the kinetic and ohmic regions of the polarization curve, a result of the intrinsically higher activity of the alloy catalyst. Performance of IL-encapsulated catalysts depends sensitively on the amount of IL used. When the volume of IL exactly equaled the porous volume of the metal nanoporous nanoparticles within the catalyst layer (0.025 μL_{IL} cm^{-2}) we noticed two effects: i) there was a slight improvement in power at low overpotential likely due to the improved ORR kinetics associated with the higher O_2 solubility of the IL; ii) performance was greatly improved at high current densities where the hydrophobicity of the IL should limit product water build up on the exterior of the composite catalyst, lowering its effect on the mass transport of reactant O_2. While encouraging, the modest increase in activity at low overpotential does not match our half-cell results, which we suspect is due to insufficient encapsulation of all of the porous particles in the catalyst layer. When a slight excess of IL was added, the activity improvement over Pt/C in the kinetic region of the polarization curve matched that measured in the half-cell, where a 60 mV positive shift was observed in each case. This reduction in overpotential for oxygen reduction is quite obvious in the kinetic region of the polarization curve where, without iR correction (inset in Figure 3A), the encapsulated catalyst architecture exhibited a nearly order of magnitude increase in activity at 0.9 V, reaching a current density of 100 mA cm^{-2}, again, with a thick Nafion membrane and a cathode loading of only 0.2 mg_{Pt} cm^{-2}. This enhancement in activity is a consequence of the local environment at the catalyst surface provided by the IL where several factors likely contribute to the overall improvement: i) the hydrophobic IL prevents water buildup at the catalyst surface; ii) it favorably adjusts the reaction kinetics by increasing O_2 residence time at the catalyst surface, increasing both attempt frequency and probability of reaction as well as ensuring full incorporation of reactant O_2 into the interior of the nanoporous catalyst; iii) in the half-cell, ORR kinetics are typically measured on nearly oxide-free Pt surfaces, by sweeping the potential anodically; however, in a PEMFC cathode, polarization curves are recorded on an OH_{ad} covered catalyst surface as the potential is swept cathodically. As we demonstrated in the half-cell, the IL reduces the degree of OH_{ad} coverage, freeing more active sites, improving the kinetics and shifting the reaction order with respect to O_2 closer to 1. Although excess IL improved PEMFC activity at lower overpotential, at high current density there was an increase in O_2 transport resistance through the catalyst layer, likely due to an excess of IL within the larger, ≈100 nm pores between the carbon supports slowing O_2 transport, suggesting that a

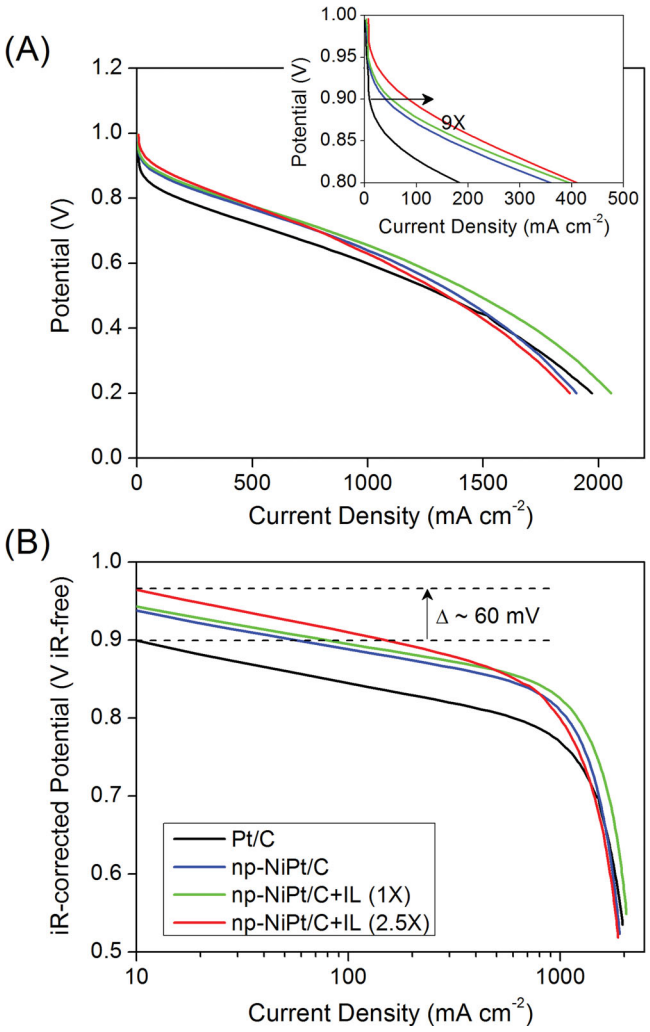

Figure 3. Polarization data for PEMFCs employing cathode catalyst layers composed of encapsulated nanoporous nanoparticle catalysts. A) Raw data polarization curves for 20 wt% Pt/C (black line), np-NiPt/C (blue line), np-NiPt/C with [MTBD][beti] IL added to the catalyst layer in a volume equal to the pore volume of the nanoporous nanoparticles in the catalyst layer (green line) and np-NiPt/C with [MTBD][beti] IL added to the catalyst layer in a volume 2.5 times the pore volume of the nanoporous nanoparticles in the catalyst layer (red line). Each MEA had an anode of 20 wt% Pt/C at 0.4 mg_{Pt} cm^{-2} and a cathode loading of 0.2 mg_{Pt} cm^{-2} of the designated catalyst. In the mass transport-limited region (above ≈1000 mA cm^{-2}), a small amount of IL helps repel water (green, 1X IL), leading to larger currents, but too much IL stymies mass transport to the catalyst surface (red, 2.5X IL) in this regime. B) iR-corrected polarization curves (0.17 Ω cm^2) compensating for ionic and electrical resistances. When using enough IL, the same 60 mV reduction in overpotential seen in the half-cell data is reflected in the positive shift in the kinetic region of the polarization curves, leading to a nearly order-of-magnitude increase in the uncorrected current density (and power) at 0.9 V compared to state-of-the-art Pt/C, as shown in the inset of (A).

direction to improve the encapsulating IL is to tailor the chemistry of the ionic species for enhanced O_2 diffusivity.

These PEMFC results represent a very preliminary investigation of integration of our composite catalyst into a cathode catalyst layer where the MEAs tested are far from optimized and proper integration will require further catalyst and catalyst layer engineering. That said, we have successfully transformed our idealized bulk composite catalyst[20] into a practical supported nanoparticle form factor and matched rotating disk electrode (RDE) half-cell activity trends within a PEMFC. Obviously, the working model of the increased activity using IL-encapsulation would be bolstered if we used an IL with higher oxygen solubility than [MTBD][beti]. While we have not yet identified such a material, it is interesting to speculate that even higher activity catalysts might be made simply by changing the nature of the organic encapsulant. After all, there are perfluoronated chemicals having O_2 solubilities greater than 50 times that of water.[63] Unfortunately, such perfluoronated chemicals typically do not also possess the requisite thermal and electrochemical stability, proton mobility, and most importantly, the lack of adsorption blocking of catalytically active sites required for the IL in the context of oxygen reduction. But in principle, an optimized catalyst encapsulation could lead to commercially relevant reductions in the required Pt loadings in PEMFCs.

3. Conclusions

We have presented the development of a novel nanostructured catalyst architecture where high surface area, nanoporous Ni/Pt alloy nanoparticles were encapsulated with a hydrophobic, protic IL. The high O_2 solubility in the IL combined with the confined environment within the pores of the catalyst led to enhanced attempt frequencies and improved ORR kinetics where the activity trends found in the half-cell were directly translated into a PEMFC. The expansive library and potential variety of organic chemical species available for use as both cations and anions of protic ILs opens the door for further improvements in activity with our encapsulated catalyst architecture where IL properties such as protonic conductivity, hydrophobicity, equilibrium water content, and oxygen solubility and diffusivity may be synthetically tuned for optimal performance.

4. Experimental Section

Carbon-supported NiPt alloy nanoporous nanoparticles were formed by dealloying ≈15 nm, $Ni_{75}Pt_{25}$ nanoparticles synthesized through the procedure outlined in previous work.[22] The central points of the synthesis are as follows: in a glove box (Labconco), 0.73 mmol Ni(II) acetylacetonate ($Ni(acac)_2$) (Sigma Aldrich, 97%), 3 mmol 1-adamantanecarboxylic acid (ACA) (Sigma Aldrich, 99%), 0.15 mmol 1,2-tetradecandiol (TDD) (Sigma Aldrich, 90%), 0.10 mmol borane-tert-butylamine (BtB) (Sigma Aldrich, 97%), 4 mL oleylamine (Sigma Aldrich, 70%), and 10 mL diphenyl ether (DPE) (Sigma Aldrich, ReagentPlus, 99%) were loaded into a four neck flask and stirred at 500 rpm under flowing argon (Roberts Oxygen, zero grade). The solution was stirred and heated to 225 °C, and then 0.27 mmol Pt(II) acetylacetonate ($Pt(acac)_2$) (Sigma Aldrich, 97%) dissolved in 3 mL dichlorobenzene (DCB) (Sigma Aldrich, 99%) was quickly injected into the solution. The solution was held at 225 °C for 60 min. and then allowed to cool to room temperature while still under an argon atmosphere. The cooled solution was then dispersed in ethanol (Pharmco-Aaper, 200 proof) and centrifuged (Thermo Scientific, CL2) to separate out the particles. Cleaned particles were loaded onto a carbon support (XC-72R, Cabot) via a colloidal deposition process to make the NiPt/C precursor material. Organic surface contaminants were removed by heating the supported catalysts at 185 °C in a tube furnace (Lindberg) under flowing O_2/Ar 10%/90% for 1 h, followed by a homogenization anneal under H_2/Ar 5%/95% (Roberts Oxygen, Zero grade) at 400 °C for 1 h. Homogenization was found to be critical for alloy stability during dealloying and subsequent oxygen reduction testing, in agreement with observations in the literature.[64–66]

The [MTBD][beti] IL was made according to the procedure outlined in previous studies.[20,24] In this procedure, equimolar amounts of the precursors 7-methyl-1,5,7-triazabicyclo[4.4.0]dec-5-ene [MTBD] (Sigma Adlrich) and the lithium salt of bis(perfluoroethylsulfonyl)imide [beti] (3M) were individually dissolved in water solutions. The [MTBD] solution was neutralized by dropwise addition of a 10.6 M HNO_3 (VWR, ACS, 70%) solution, cooled in ice to near 0 °C in order to limit heat released during the exothermic reaction. After neutralization, the Li [beti]/water solution was mixed with the neutralized [MTBD], and the IL precipitated out as a viscous fluid phase beneath a water phase containing dissolved $LiNO_3$. The IL was washed several times with DI water and then placed in a vacuum oven at 70 °C for 24 h to remove residual water.

Homogenized NiPt/C nanoparticle catalysts were dealloyed, electrochemically characterized and assessed for oxygen reduction activity in a three electrode cell with a Pt mesh (Alfa Aesar) counter electrode and a Hg/Hg_2SO_4 (mercury/mercury sulfate electrode; MSE) reference electrode. The reference electrode was calibrated against a hydrogen reference and found to have an offset of 0.716 V at 25 °C, 0.710 V at 45 °C. and 0.706 V at 60 °C. The Hg/Hg_2SO_4 potential offset was further confirmed by multiple comparisons to other reference electrodes, as well as to the positions of characteristic peaks for H_{UPD} and Pt oxidation/reduction found in the literature.[67,68] Prior to any electrochemical experiments, all glassware was cleaned by soaking a solution of concentrated H_2SO_4 (J. T. Baker, ACS grade) and Nochromix cleaner (Godax Laboratories, Inc.) for at least eight hours followed by through rinsing in Millipore water. All solutions were made using Millipore (MilliQ Synthesis A10) water with a resistivity greater than 18.2 MΩ cm.

Supported catalysts were dispersed in a 4:1 H_2O:IPA volume solution at a concentration of 3 $mg_{catalyst}$ mL^{-1}, 0.4 µL $mg_{catalyst}^{-1}$ of a 5 wt% Nafion/IPA solution was added to the catalyst ink to aid in dispersion and adhesion of the catalyst particles to the glassy carbon (GC) disk (5 mm diameter, 0.196 cm^2, Pine Instruments). The GC disk, prior to loading with catalyst, was polished to a mirror finish using 0.1 micrometer diamond paste (Buehler) followed by sonication in Millipore water to remove contaminants. An appropriate volume of catalyst ink for a 12 μg_{Pt} cm^{-2} loading was pipetted onto the GC disk and dried under a flow of argon to form a uniform layer. This is the loading used in all half-cell measurements. Great care was taken in order to form a homogeneous film as catalytic activity is strongly correlated to the quality of the catalyst layer on the disk.[41,42] Dealloying was performed in N_2-purged (Roberts Oxygen, Zero grade) 0.1 M $HClO_4$ by cycling the potential between 0.05 and 1.2 V versus RHE (Gamry 750 mA potentiostat) at 250 mV s^{-1} for at least 50 cycles; all quantitative cyclic voltammograms (CV) used a sweep rate of 50 mV s^{-1}. The ECSAs of the dealloyed catalysts were found through integration of the current in the hydrogen underpotential deposition (H_{UPD}) region of the CVs, specifically the hydrogen adsorption region of the curve, subtracting out the non-Faradaic current associated with double layer charging and assuming 210 µC cm_{Pt}^{-2}. After the catalyst was fully dealloyed, it was rinsed thoroughly in Millipore water and transferred to O_2 (Roberts Oxygen, Research grade) saturated 0.1 M $HClO_4$ at the desired temperature for measurement of the ORR activity. Using a Pine Instruments rotator (AFMSRCE), the GC disk was rotated at a desired rpm while running linear sweep voltammetry from 0.1 to 1.1 V versus

RHE at 20 mV s^{-1}. Current-voltage data was corrected for ohmic iR drop using the procedure outlined in previous work.[69]

To make sufficient quantities of the cathode catalyst for fuel cell tests, NiPt/C precursor material was collected on a gold dish electrode and then dealloyed in 0.1 M $HClO_4$ via potential cycling. In this way, hundreds-of-milligram quantity batches of np-NiPt/C were produced, and the method can easily be scaled up to produce larger scale batches. Dealloyed catalysts were subsequently cleaned through sonication in ultrapure water and then dried under flowing argon. The resulting np-NiPt/C catalysts had an average metal loading of 30 wt% on the carbon support and a residual Ni content of 35 at.%. Half-cell RDE tests of np-NiPt/C produced in this manner showed identical catalytic activity as materials produced by dealloying the precursor on a GC disk.

Encapsulated nanoporous nanoparticle catalysts were made by dispersing the supported catalyst in isopropanol through sonication with the desired volume of IL followed by evaporation of the isopropanol. Catalyst ink was made by dispersing an appropriate amount of dry catalyst in a 3:1 vol/vol mixture of ethanol:water to make a solution that is 5 wt% solids. Following sonication in an ice bath for 30 min, a 5 wt% solution of Nafion (Ion Power) was added to the ink in a quantity that would produce a dried catalyst layer containing 33 wt% Nafion,[70–72] followed by further sonication in the ice bath for 30 min. Membrane electrode assemblies (MEA) were fabricated by hand painting the catalyst ink onto the microporous layer side of a gas diffusion layer (Avcarb, Ballard) (GDL) followed by hot pressing of two catalyst loaded GDLs onto either side of a dry Nafion 115 membrane (Ion Power), 0.125 mm thick, at a pressure of 44 MPa and temperature of 150 °C for 30 s. Thicker Nafion was used to limit H_2 crossover, facilitating analysis of data in the kinetic region, high potential and low current density, of the polarization curves. Prior to hotpressing, as-received Nafion membranes were cleaned by boiling in 3 wt% hydrogen peroxide (Fisher Scientific, 30 wt%) for one hour, boiling in Millipore water for one hour and finally boiling in 1 M H_2SO_4 for one hour. The Nafion membranes were washed thoroughly with Millipore water after each step. The cathode catalyst layer consisted of 20 wt% Pt/C, np-NiPt/C or np-NiPt/C+[MTBD][beti] at a loading of 0.2 mg_{Pt} cm^{-2}. Commercial 20 wt% Pt/C (Johnson Matthey) was used as the anode catalyst with a loading of 0.4 mg_{Pt} cm^{-2} to ensure that the cathode reaction was the limiting reaction.

The MEAs, with a geometric electrode surface area of 2 cm^2, were placed between graphite serpentine flow fields and their fuel cell performance was assessed using an 850C fuel cell test station (Scribner Associates). The fuel cell was operated with H_2/O_2 (0.5 L min^{-1}/1.0 L min^{-1}) at 175 kPa back pressure, 100% relative humidity and a stack temperature of 80 °C. O_2 was used rather than air to facilitate direct comparison between the half-cell and PEMFC results. Prior to the recording of any polarization curves, the MEAs were taken through a short break-in/stability protocol, after the fuel cell was properly heated and kept under continuous reactant flow for at least 2 h, consisting of 3000 potential hold steps between 0.6 V and 1.0 V where each step had a duration of 5 s. Resistivity of the MEA, graphite flow fields and current collector plates was experimentally determined for iR correction using a Solartron FRA with an AC amplitude of 100 mV and a frequency range from 1 Hz to 10 kHz. Values, a sum of ionic and electrical resistances, for our MEAs and fuel cell setup averaged around 0.17 Ω cm^2.

The microstructure of the dealloyed and IL encapsulated nanoparticles was visually characterized using transmission electron microscopy. TEM was performed on a 300 kV, field-emission Philips CM300-FEG TEM at the Electron Microscopy Center at Johns Hopkins University. An EDAX EDS (Energy Dispersive Spectroscopy) X-ray microanalysis system on the TEM was used to measure Ni and Pt fractions in the nanoparticle samples.

TEM sample preparation for both encapsulated and bare nanoporous nanoparticles were identical. Specifically, nanoparticles were dispersed in Millipore water through ultrasonication and lacey-carbon TEM grids were dipped into the suspensions and allowed to dry for approximately 10 min before placing into the TEM. Because of the potential for contamination build up during TEM imaging, both sets of images (Figure 1; Figure S1, Supporting Information) were obtained on areas with minimal beam exposure (less than 1 min). After the initial images were taken, the beam was allowed to rest on the same areas in order to determine if contamination would appear or increase. In both cases, no contamination build up was observed, confirming that the amorphous coating on the encapsulated NPs is not from contamination. In addition, the thickness of the IL layer was stable under the high resolution TEM imaging conditions used to obtain Figure 1.

Supporting Information

Supporting Information is available from the Wiley Online Library or from the author.

Acknowledgements

The authors would like to thank Dr. Yossef Elabd in the Chemical and Biological Engineering Department at Drexel University for use of the fuel cell testing facilities. The authors acknowledge funding from the U.S. Department of Energy, Basic Energy Sciences, grant DE-SC0008686.

Received: April 3, 2013
Revised: April 23, 2013
Published online: June 12, 2013

[1] I. Stephens, A. Bondarenko, U. Gronbjerg, J. Rossmeisl, I. Chorkendorff, *Energy Environ. Sci.* **2012**, *5*, 6744.
[2] V. Stamenkovic, B. Fowler, B. Mun, G. Wang, P. Ross, C. Lucas, N. Markovic, *Science* **2007**, *315*, 493.
[3] J. Kim, S. Lee, C. Carlton, Y. Shao-Horn, *Electrochem. Solid-State Lett.* **2011**, *14*, B110.
[4] J. Wu, J. Zhang, Z. Peng, S. Yang, F. Wagner, H. Yang, *J. Am. Chem. Soc.* **2010**, *132*, 4984.
[5] J. Zhang, H. Yang, J. Fang, S. Zou, *Nano Lett.* **2010**, *10*, 638.
[6] D. van der Vliet, C. Wang, M. Debe, R. Atanasoski, N. Markovic, V. Stamenkovic, *Electrochim. Acta* **2011**, *56*, 8695.
[7] C. Wang, D. van der Vliet, K. Chang, H. You, D. Strmcnik, J. Schlueter, N. Markovic, V. Stamenkovic, *J. Phys. Chem. C* **2009**, *113*, 19365.
[8] J. Wu, H. Yang, *Nano Res.* **2011**, *4*, 72.
[9] C. Wang, M. Chi, D. Li, D. van der Vliet, G. Wang, Q. Lin, J. Mitchell, K. More, N. Markovic, V. Stamenkovic, *ACS Catal.* **2011**, *1*, 1355.
[10] M. Carpenter, T. Moylan, R. Kukreja, M. Atwan, M. Tessema, *J. Am. Chem. Soc.* **2012**, *134*, 8535.
[11] J. Wang, H. Inada, L. Wu, Y. Zhu, Y. Choi, P. Liu, W. Zhou, R. Adzic, *J. Am. Chem. Soc.* **2009**, *131*, 17298.
[12] V. Stamenkovic, B. Mun, K. Mayrhofer, P. Ross, N. Markovic, *J. Am. Chem. Soc.* **2006**, *128*, 8813.
[13] J. Zhang, Y. Mo, M. Vukmirovic, R. Klie, K. Saski, R. Adzic, *J. Phys. Chem. B* **2004**, *108*, 10955.
[14] K. Kuttiyiel, K. Sasaki, Y. Choi, D. Su, P. Liu, R. Adzic, *Energy Environ. Sci.* **2012**, *5*, 5297.
[15] P. Strasser, S. Koh, T. Anniyev, J. Greeley, K. More, C. Yu, Z. Liu, S. Kaya, D. Nordlund, H. Ogasawara, M. Toney, A. Nilsson, *Nat. Chem.* **2010**, *2*, 454.
[16] C. Wang, M. Chi, D. Li, D. Strmcnik, D. van der Vliet, G. Wang, V. Komanicky, K. Chang, A. Paulikas, D. Tripkovic, J. Pearson, K. More, N. Markovic, V. Stamenkovic, *J. Am. Chem. Soc.* **2011**, *133*, 14396.

[17] C. Wang, M. Chi, G. Wang, D. van der Vliet, D. Li, K. More, H. Wang, J. Schlueter, N. Markovic, V. Stamenkovic, *Adv. Funct. Mater.* **2011**, *21*, 147.
[18] C. Wang, G. Wang, D. van der Vliet, K. Chang, N. Markovic, V. Stamenkovic, *Phys. Chem. Chem. Phys.* **2010**, *12*, 6933.
[19] J. Snyder, K. Livi, J. Erlebacher, *J. Electrochem. Soc.* **2008**, *155*, C464.
[20] J. Snyder, T. Fujita, M. W. Chen, J. Erlebacher, *Nat. Mater.* **2010**, *9*, 904.
[21] J. Greely, I. Stephens, A. Bondarenko, T. Johansson, H. Hansen, T. Jaramillo, J. Rossmeisl, I. Chorkendorff, J. Norskov, *Nat. Chem.* **2009**, *1*, 552.
[22] J. Snyder, I. McCue, K. Livi, J. Erlebacher, *J. Am. Chem. Soc.* **2012**, *134*, 8633.
[23] I. McCue, J. Snyder, X. Li, Q. Chen, K. Sieradzki, J. Erlebacher, *Phys. Rev. Lett.* **2012**, *108*, 225503.
[24] H. Luo, G. Baker, J. S. Lee, R. M. Pagni, S. Dai, *J. Phys. Chem. B* **2009**, *113*, 4181.
[25] A. Noda, A. Susan, K. Kudo, S. Mitsushima, K. Hayamizu, M. Watanabe, *J. Phys. Chem. B* **2003**, *107*, 4024.
[26] C. Ke, J. Li, X. Li, Z. Shao, B. Yi, *RSC Adv.* **2012**, *2*, 8953.
[27] J. Rollins, J. Conboy, *J. Electrochem. Soc.* **2009**, *156*, B943.
[28] T. Yasuda, A. Ogawa, M. Kanno, K. Mori, K. Sakakibara, M. Watanabe, *Chem. Lett.* **2009**, *38*, 692.
[29] S. Lee, A. Ogawa, M. Kanno, H. Nakamoto, T. Yasuda, M. Watanabe, *J. Am. Chem. Soc.* **2010**, *132*, 9754.
[30] T. M. Chang, L. X. Dang, R. Devanathan, M. Dupuis, *J. Phys. Chem. A* **2010**, *114*, 12764.
[31] R. Hayes, S. Imberti, G. Warr, R. Atkin, *Angew. Chem. Int. Ed.* **2012**, *51*, 7468.
[32] M. Kim, C Glinka, S. Grot, W. Grot, *Macromolecules* **2006**, *39*, 4775.
[33] H. Haubold, T. Vad, H. Jungbluth, P. Hiller, *Electrochim. Acta* **2001**, *46*, 1559.
[34] T. Greaves, D. Kennedy, A. Weerawardena, N. Tse, N. Kirby, C. Drummond, *J. Phys. Chem. B* **2011**, *115*, 2055.
[35] M. Anouti, J. Jaquemin, P. Porin, *J. Phys. Chem. B* **2012**, *116*, 4228.
[36] P. Choi, N. Jalani, R. Datta, *J. Electrochem. Soc.* **2005**, *152*, E123.
[37] S. Paddison, R. Paul, *Phys. Chem. Chem. Phys.* **2002**, *4*, 1158.
[38] A. Sacca, A. Carbone, R. Pedicini, G. Portale, L. D'Ilario, A. Longo, A. Martorana, E. Passalacqua, *J. Membr. Sci.* **2006**, *278*, 105.
[39] M. Nesselberger, S. Ashton, J. Meier, I. Katsounaros, K. Mayrhofer, M. Arenz, *J. Am. Chem. Soc.* **2011**, *133*, 17428.
[40] K. Ke, K. Hiroshima, Y. Kamitaka, T. Hatanaka, Y. Morimoto, *Electrochim. Acta* **2012**, *72*, 120.
[41] Y. Garsany, I. Singer, K. Swider-Lyons, *J. Electroanal. Chem.* **2011**, *662*, 396.
[42] Y. Garsany, O. Baturina, K. Swider-Lyons, S. Kocha, *Anal. Chem.* **2010**, *82*, 6321.
[43] M. Shao, K. Shoemaker, A. Peles, K. Kaneko, L. Protsailo, *J. Am. Chem. Soc.* **2010**, *132*, 9253.
[44] I. Dutta, M. Carpenter, M. Balogh, J. Ziegelbauer, T. Moylan, M. Atwan, N. Irish, *J. Phys. Chem. C* **2010**, *114*, 16309.
[45] Y. Liu, C. Hangarter, U. Bertocci, T. Moffat, *J. Phys. Chem. C* **2012**, *116*, 7848.
[46] J. Kibsgaard, Y. Gorlin, Z. Chen, T. Jaramillo, *J. Am. Chem. Soc.* **2012**, *134*, 7758.
[47] R. Wang, C. Xu, X. Bi, Y. Ding, *Energy Environ. Sci.* **2012**, *5*, 5281.
[48] D. Zhang, T. Okajima, F. Matsumoto, T. Ohsaka, *J. Electrochem. Soc.* **2004**, *151*, D31.
[49] J. Bae, J. Han, T. Chung, *Phys. Chem. Chem. Phys.* **2012**, *14*, 448.
[50] J. Han, E. Lee, S. Park, R. Chang, T. Chung, *J. Phys. Chem. C* **2010**, *114*, 9546.
[51] V. Sehuraman, S. Khan, J. Jur, A. Haug, J. Weidner, *Electrochim. Acta* **2009**, *54*, 6850.
[52] S. Gottesfeld, I. D. Raistrick, S. Srinivasan, *J. Electrochem. Soc.* **1987**, *134*, 1455.
[53] S. K. Zecevic, J. S. Wainright, M. H. Litt, S. L. Gojkovic, R. F. Savinell, *J. Electrochem. Soc.* **1997**, *144*, 2973.
[54] Z. Ogumi, Z. Takehara, S. Yoshizawa, *J. Electrochem. Soc.* **1984**, *131*, 769.
[55] A. Parthasarathy, C. Martin, S. Srinivasan, *J. Electrochem. Soc.* **1991**, *138*, 916.
[56] A. Ayad, Y. Naimi, J. Bouet, J. Fauvarque, *J. Power Sources* **2004**, *130*, 50.
[57] R. Subbaraman, D. Strmcnik, A. Paulikas, V. Stamenkovic, N. Markovic, *ChemPhysChem* **2010**, *11*, 2825.
[58] R. Subbaraman, D. Strmcnik, V. Stamenkovic, N. Markovic, *J. Phys. Chem. C* **2010**, *114*, 8414.
[59] H. Chen, J. Snyder, Y. Elabd, *Macromolecules* **2008**, *41*, 128.
[60] G. Gruver, R. Pascoe, H. Kunz, *J. Electrochem. Soc.* **1980**, *127*, 1219.
[61] H. Colon-Mercado, B. Popov, *J. Power Sources* **2006**, *155*, 253.
[62] H. Colon-Mercado, H. Kim, B. Popov, *Electrochem. Comm.* **2004**, *6*, 795.
[63] M. Gomes, J. Deschamps, D. Menz, *J. Fluorine Chem.* **2004**, *125*, 1325.
[64] L. Gan, M. Heggen, R. O'Malley, B. Theobald, P. Strasser, *Nano Lett.* **2013**, *13*, 1131.
[65] L. Gan, M. Heggen, S. Rudi, P. Strasser, *Nano Lett.* **2012**, *12*, 5423.
[66] M. Oezaslan, M. Heggen, P. Strasser, *J. Am. Chem. Soc.* **2012**, *134*, 514.
[67] U. Paulus, A. Wokaun, G. Scherer, T. Schmidt, V. Stamenkovic, N. Markovic, P. Ross, *Electrochim. Acta* **2002**, *47*, 3787.
[68] K. Mayrhofer, D. Strmcnik, B. Blizanac, V. Stamenkovic, M. Arenz, N. Markovic, *Electrochim. Acta* **2008**, *53*, 3181.
[69] D. van der Vliet, D. Strmcnik, C. Wang, V. Stamenkovic, N. Markovic, M. Koper, *J. Electroanal. Chem.* **2010**, *647*, 29.
[70] G. Sasikumar, J. W. Ihm, H. Ryu, *Electrochim. Acta* **2004**, *50*, 601.
[71] S. Mu, M. Tian, *Electrochim. Acta* **2012**, *60*, 437.
[72] Z. Qi, A. Kaufman, *J. Power Sources* **2003**, *113*, 37.